Optical energy transfer of gold plasmonic antennas

Masters Thesis
Applied Physics

J.J.F. van 't Oever

Supervisors
Prof.dr. J.L. Herek
Dr.ir. H.L. Offerhaus

M.Sc. committee
Dr.ir. A.P. Mosk
D.J.W. Dikken M.Sc.

Optical Sciences
Faculty of Science and Technology
University of Twente
Enschede, 13 October 2011

Contents

Chapter 1

Acknowledgments

First of all I would like to thank a few people for their help and support during my Master's project. I would like to thank Frans for the insights on and the efforts made for the fabrication of gold nanostructures and the discussions on the social-economic state of the world. Frans is, together with Jeroen Korterik, part of another invaluable part of the group which I would like to thank: technical support of all kinds. I thank Dirk-Jan for his help with the synthesis of flakes and the many discussions on plasmonic resonances. Special thanks go out to Herman and Jennifer for their guidance and their own special way of creating a good atmosphere in the group. All members of Optical Sciences are thanked for providing such colorful and fruitful environment for fun and science. Last on I would like to thank Coby for keeping up with me while I invested so much time working on my project.

Chapter 2

Introduction

In his famous 1857 Bakerian lecture titled 'Experimental Relations of Gold (and other metals) to Light' [1], Michel Faraday illustrated his work on colloids with suspended gold particles, or as he called them: gold sols. Gold sols had then been known from alchemists for two centuries but Faraday was the first to present a scientific study on their formation and properties.

Faraday showed that if the conditions were well controlled, part of the gold was reduced into highly fine particles which produced a beautiful ruby fluid. However, by adding salts the ruby fluid could be changed into a deep blue or violet fluid, or any color in between, without any gold being redissolved. Faraday concluded that this could be attributed to a change in size of the particles by a certain mechanism, as he stated:

> "There is probably some physical change in the condition of the particles, caused by the presence of the salt and such affecting media, which is not a change of the gold as gold, but rather a change of the relation of the surface of the particles to the surrounding medium."

Not only had he shown that gold nanoparticles show significantly different behavior than the bulk, that the variation of colors was due to some variations in geometry, but at the same time he conducted the first experiments on the manipulation of metallic particles on the nanoscale, thereby initiating the fields of nanotechnology and nanoscience, all this more than 150 years ago.

Since the days of Faraday our understanding of the optical response of gold nanoparticles has improved tremendously. In the beginning of the 20th century, Maxwell and Garnett explained the scattering effects and color changes in small metal particles and Mie quantitatively explained the strong size dependence on the optical properties. Several decades later also anisotropic

particles were found in photographic emulsions and their optical interactions were explained by Gans' theory.

The realization that plasmon properties are largely controlled by the shape of a metal structure at subwavelength dimensions, has boosted interest in plasmon-based phenomena, especially during last decade [2]. Although experiments and applications of plasmonics have thrived in the infrared (IR) and near infrared (NIR) fraction of the electromagnetic spectrum, experiments at optical (visible) wavelengths have posted serious limits on the feasibility of, for instance, a plasmonic all-optical chip or plasmonic metamaterials for visible wavelengths of light. The reason for this is twofold:

1. The small feature size of such structures makes reliable fabrication of such structures challenging;

2. Significant absorption of plasmon energy in the structures due to intrinsic material loss at optical frequencies makes energy loss an important and limiting effect.

One of the envisioned applications of plasmonics is to bring the well established field of radiowave and microwave technology into the visible spectrum [3]. Since the characteristic dimensions of an antenna are on the order of the radiation wavelength, fabrication accuracy down to a few nanometers is required. Due to intensive research in the areas for the nanotechnology and nanoscience, several fabrication methods such as focused ion beam (FIB) [4] milling, electron-beam lithography [5] or by self-assembly [6] have been successfully using to fabricate nanoantennas.

One of the fundamental examples of antenna technology is the well known half wavelength or dipole antenna. A transmitting antenna consists of two conductors of length $L/4$, connected by a sinusoidally varying current source. In this case electromagnetic waves with a wavelength $\lambda = 2 \cdot L$ will radiate away from the antenna. Due to the reciprocity of this electromagnetic problem, the same antenna will also act as an efficient receiver for these waves and convert it into a current.

When the dipole antenna is scaled down towards visible and NIR wavelengths (380 - 1400 nm), the antenna losses increase significantly. Due to the skin effect, the induced current can be described as a localized plasmonic resonance and the classic scaling law for the half wave antenna is not valid anymore and the actual length becomes much smaller [7]. The coherent oscillation of the conduction electrons in a gold or silver antenna dephases by a variety of processes, such as electron-phonon coupling (conversion into heat) or electron-electron scattering, such as excitation into a empty levels

in the conduction band (interband transitions) or from the d-band into the conduction band (intraband transitions). These effects are entirely described by the electric permittivity of the material [8]. When the particles become larger, the plasmon oscillation can also lose energy by radiation coupling and a scattering field is generated [9].

To reduce the damping of the plasmon resonance in optical antennas, two approaches are used in this work. To reduce the the radiation losses, the dipole antenna is coupled to a non-radiating antenna mode of a nanoring placed next to the antenna, thereby storing the field energy into a non-radiating mode. If this proves to be successful, the energy could possibly be guided away from the dipole antenna using a chain of rings or other particles [10, 11]. Secondly, a new method of gold substrate fabrication using chemically synthesized single-crystal gold flakes is developed.

Chapter 3

Theory of Plasmons

To aid the design of plasmonic nanostructures a solid, fundamental understanding of the phenomena is necessary. In this chapter several approaches to describe plasmons are presented.

3.1 Plasmons

First of all, what is a 'plasmon'? Imagine a perfectly conducting cube on which an external, static electric field is applied from left to right. The free electrons in the metal feel the Coulomb force and collectively move to the left, creating a negative surface charge on the left side of the cube and leaving a positive surface charge on the right side, such that the total field inside the cube is zero. Now if the field is switched off, the electrons are repelled from the left side and attracted to the right side of the cube and the electron density starts oscillating back and forth around the equilibrium position with a characteristic frequency called the plasma frequency [12]:

$$\omega_p = \sqrt{\frac{n_e e^2}{m_e^* \epsilon_0}} \tag{3.1}$$

where n_e is the conduction electron density, e is the elementary charge, m_e^* the effective electron mass and ϵ_0 the permittivity of free space. A plasmon is a quantization of this collective, longitudinal oscillation of the free electron plasma of a metal or semiconductor.

3.2 Antenna theory

Another approach to describe the optical interaction of light with a metallic nanoparticle is to describe it as an antenna. In traditional antenna design,

structures are used which have characteristic lengths that optimized for a certain wavelength. For example, an ideal half-wave dipole antenna consists of a small metallic rod with a radius $R << \lambda$ and a length L

$$L = \frac{\lambda}{2}. \tag{3.2}$$

However, when a classical antenna is scaled down such that it should be resonant for electromagnetic fields at optical frequencies (e.g. visible light), the simple scaling breaks down because the penetration of the fields into the material cannot be neglected and formula 3.2 is not valid anymore. Because of the small size of the antenna, the skin effect has a significant effect on the effective impedance (or equivalently the complex index of refraction) of a electromagnetic wave on the antenna. The penetration of the incident wave generates density fluctuations in the free electron density close the surface, so this is in fact a plasmonic effect [7].

If the effect of the plasmons would be included in the calculation of the effective wavelength for a cylindrical antenna of radius r, a linear scaling law can be found [7]:

$$\lambda_{eff} = \frac{\lambda}{\sqrt{\epsilon_s}} \sqrt{\frac{4\pi^2 \epsilon_s (r^2/\lambda^2) \widetilde{z}^2}{1 + 4\pi^2 \epsilon_s (r^2/\lambda^2) \widetilde{z}^2}} - 4r \tag{3.3}$$

$$\widetilde{z} = a_1 + a_2 \frac{\lambda}{\lambda_p} \tag{3.4}$$

$$a_1 = \frac{1}{3} e^{\zeta} \left[1 + \frac{\sqrt{3\zeta}}{2} \right] - \frac{2\left(\epsilon_\infty + \epsilon_s e^{2\zeta}/2\right)}{3\epsilon_s e^{\zeta}} \left[1 + \frac{\sqrt{3}}{2} \frac{1+\zeta}{\sqrt{\zeta}} \right] \tag{3.5}$$

$$a_2 = \frac{2\sqrt{\epsilon_\infty + \epsilon_s e^{2\zeta}/2}}{3\epsilon_s e^{\zeta}} \left[1 + \frac{\sqrt{3}}{2} \frac{1+\zeta}{\sqrt{\zeta}} \right] \tag{3.6}$$

$$\zeta = \frac{5}{3} + 2\gamma \tag{3.7}$$

where λ_{eff} is the effective wavelength, ϵ_∞ and λ_p are the electric permittivity at infinite wavelength and the plasma wavelength of the antenna material, ϵ_s is electric permittivity of the surrounding medium, R is the antenna radius and γ is Euler's constant. For gold at optical frequencies, $\epsilon_\infty \approx 11$ F/m and $\lambda_p \approx 138$ nm.

For a plasmonic half wavelength antenna of radius r, the resonance condition now becomes

$$L = \frac{1}{2} \lambda_{eff} \tag{3.8}$$

where L is the length of the nanoantenna and λ_{eff} is the effective wavelength as calculated with formula 3.3.

In case of a plasmonic ring antenna, the plasmon resonances on the ring can be described as standing waves formed by plasmon resonances on a infinite cylinder of radius r [11, 13]. In this case the resonance conditions for a plasmonic nanoring becomes

$$R = \frac{N \cdot \lambda_{eff}}{2\pi} \tag{3.9}$$

where R is the radius of ring, r is the radius of the cross section of the ring wall, N is the number of plasmonic wavelengths on the ring and λ_{eff} is the effective wavelength as calculated with formula 3.3. $N = 1$ for the dipolar mode, $N = 2$ for the quadrupole mode, etc.

Chapter 4

Finite Difference Simulations

4.1 Introduction

The electromagnetic field in problems with arbitrarily shaped nanoparticles is often of such complexity that numerical methods have to be used to predict the optical interaction of such particle with a light field. Numerical methods for this purpose have been developed in the field of computational electromagnetics as early as 1964 for the discrete dipole approximation (DDA) method [14], however only in last decade did numerical methods gain widespread use due to a tremendous increase in computational power and the development of new methods such as the finite difference in time domain method (FDTD) and the boundary element method (BEM). These three techniques are the most widely used numerical methods for the calculation of the electromagnetic response of nanostructures.

The basis of the boundary element method method is the fact that the electromagnetic field in a homogeneous volume can be determined by the fields and their derivatives, or equivalently by the charge and current distribution, on the surface of the volume. By expressing and discretizing the scattered fields in terms of charges and current distributions and combining them with the Maxwell boundary conditions leads to a system of linear equations which can be solved using normal linear algebra methods.

In the discrete dipole approximation the metal is described by a lattice of coupled point dipoles where the lattice can be shaped in any shape. An electric field is imposed on the dipoles in the frequency domain and the resulting polarization of each dipole resulting from the external field and the local fields produced by the other dipoles is calculated, from which a total polarization as function of frequency can be derived.

The finite difference time domain method relies on a step-wise calculation

of the propagation of an incident electromagnetic field through a discretized simulation space called a Yee latice. The name is derived from the fact that this method approximates the time and space derivatives of the fields by finite differences by discretizing the fields on a Yee cell (see figure 4.1). During each time step, the updated value for the electric field is calculated from the previous value and the numerical curl of the magnetic fields (and vice versa for the magnetic field) for all points in space. This method of choosing how the curls should be calculated has been proposed by Yee in 1966 and has shown to be very robust [15]. Therefore it is used as the basis for most software implementations of FTTD.

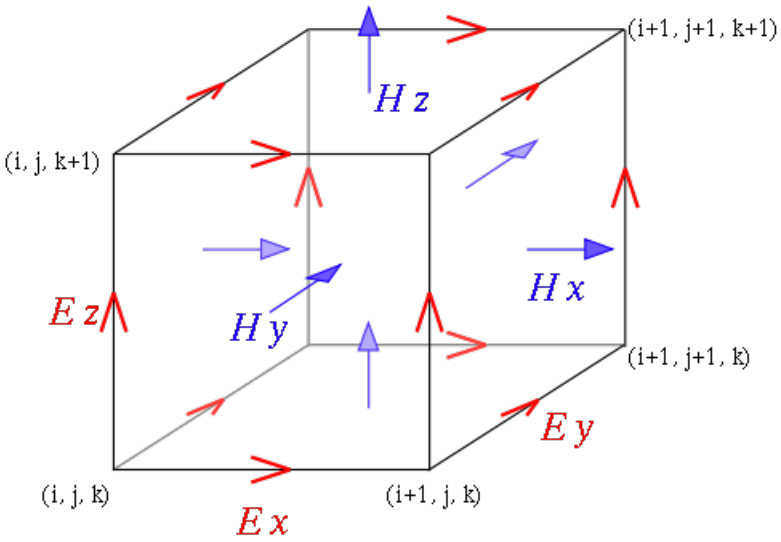

Figure 4.1: A Yee cube illustrating the distribution of the electric and magnetic fields used for discretizing the fields in FDTD simulations [16]

Not only the structure of interest but also a sufficiently large surrounding medium has to be discretized in case of FDTD simulations to allow for the source field to accurately reach the structure and to give the generated scattered field space to propagate away from the structure. The surrounding space is typically as large as the near-field, so depending of the wavelength range of interest. In these simulations a surrounding space of 1.2 μm is used in all three dimensions. Using near-field to far-field transformations, the far-field response of a near-field simulation can be simulated. An important advantage of the FDTD method is the use of a pulsed excitation wave, such that the response on all frequency components can be simulated in one single simulation run.

4.2 Implementation in CST Microwave Studio

CST Microwave Studio (CST) is a software package for FDTD simulations. It consists of a graphical user interface, with which structures can be defined in a CAD-like manner. All structures can be parameterized, such that the structures can generated with varying parameters without manually setting up the whole simualtion. All simulations were performed on a PC with a quadcore CPU running at 2.9 GHz, 16 GB DDR3 RAM and CST Studio Suite 2011.

4.2.1 Meshing methods

The most delicate parameter in the simulation process is the discretization or 'meshing' of the simulation domain. The mesh must strike a balance between a fine enough mesh to resolve all relevant geometrical details and a practical utilization of computational resources and simulation runtime. CST offers two automatic strategies for mesh optimization, namely the 'expert system' method and the 'energy based' method.

Expert system

The 'expert system' (ES) strategy is an iterative method to find an optimum mesh density for a certain problem. First, the problem must be defined in terms of geometry, materials, boundary conditions of the simulation domain, source fields, a relatively coarse mesh and a success parameter. The success parameter is a measurable quantity, such as a resonance frequency or extinction cross section, which is to be calculated after each simulation run. Multiple simulation runs are performed where after each run the mesh is homogeneously refined (a constant mesh density within the same material), the success parameter and the difference with the previous value of the parameter is calculated. If the difference is smaller than a user set threshold, the optimization is stopped.

The advantage of the ES method is that once optimized settings for the mesh are found, the same settings can be applied for comparable problems, as long as there are not significant differences in the field distribution.

To asses the usability of the method in terms of accuracy and computation resources, a simulation of the optical interaction of a gold antenna in vacuum is performed with ES mesh optimization. The antenna is modeled as a cylinder with a length of 110 nm, a radius of 10 nm and is described

by a first order Drude model to increase simulation speed. Interband transitions at shorter wavelengths are therefore not included in the model, but for sake of comparison of meshing methods this poses no problem. A sufficiently broadband pulsed planewave, incident at normal angle to the cylinder's axis, is used as source. For each run, the far-field extinction cross section is calculated as function of frequency. Twenty subsequent runs were performed and five resulting simulation results are shown in figure 4.2.

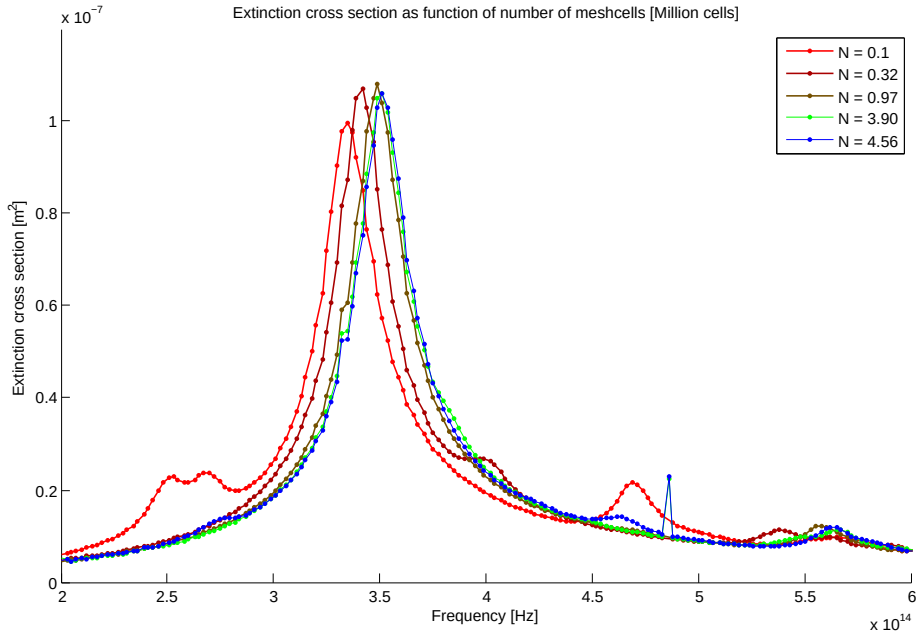

Figure 4.2: Extinction cross section of a single gold cylinder in vacuum as function of mesh optimization run using the expert system method

From the results shown in figure 4.2 several conclusions can be drawn. In terms of characteristics of the main dipole resonance, such as resonance strength, frequency and linewidth, the mesh with a total of $N = 0.96 \cdot 10^6$ meshcells is already accurate within less than 2 percent as compared with the result with $N = 4.56 \cdot 10^6$ meshcells. Performing the same comparison for the smaller resonance around $\nu = 5.6 \cdot 10^{14}$ Hz, the difference with the most accurate result is less than 5 percent. However, the two finest meshes, with $N = 3.90 \cdot 10^6$ and $N = 4.56 \cdot 10^6$ meshcells respectively, do not overlap completely suggesting full convergence has not occurred, not even with these dense meshes (corresponding with a meshstep of 1 nm in the metal and 2.7 nm in the surrounding medium). The narrow spike at the right side of the spectrum is a computational artifact, likely to stem from a scaling problem in the post-processing of data in CST.

Simulation run	Meshcells [millions]	Solver time [min]
1	0.1	4.5
5	0.32	12.5
10	0.97	32
19	3.90	135
20	4.56	172

Table 4.1: Simulation times during ES meshing optimization

If only the main dipole resonance is of interest, the ES method can be an efficient meshing method which gives a reasonable accurate mesh with the least amount of meshcells for a certain desired accuracy. If also smaller resonances are of interest or a higher degree of accuracy is required, this method does not give satisfying results since accurate convergence requires a very dense mesh. Since the example shown here is of small scale, using this method for larger scale nanostructures such as multiple particles would require an tremendous amount of simulation time (see table 4.1) and a different meshing method might be advantageous.

Energy based

The 'energy based' (EB) method is the same as the ES strategy but increases the mesh density only there, where a high energy density has been simulated. In this case the mesh density is not necessarily constant within the geometry of the nanoparticle nor within the surrounding space as is the case with the ES method and the mesh is only refined there were it is contributing most to a optimum mesh. At least one run is needed to adapt the mesh to the energy distribution of the nanostructure and as opposed to the ES method, mesh settings cannot be reused since the adaptation has to be carried out for every structure.

The same simulation is performed as described in previous section, except the meshing method is changed to Energy Based. Every subsequent run, the amount of meshcells is increased by seventy percent as compared with the previous run. A total of seven runs are performed and the results of the five most interesting results are shown in figure 4.2.

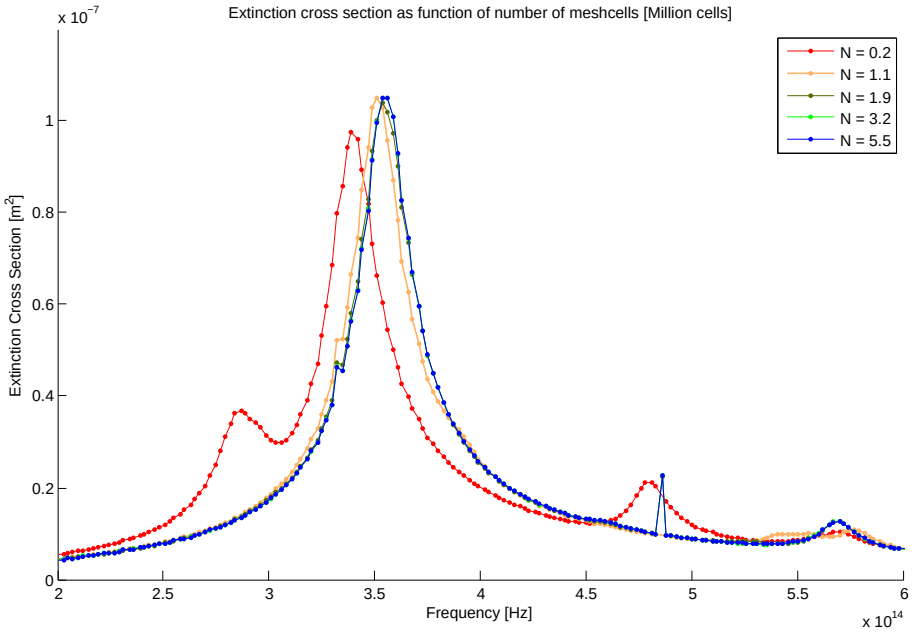

Figure 4.3: Extinction cross section of a single gold cylinder in vacuum as function of mesh optimization run using the energy based method

When compared with the ES method, the EB method converges much faster in terms of meshcells and simulation runs. The last three iterations produce very similar results, such that the run with $N = 3.2 \cdot 10^6$ meshcells is almost hidden under the most accurate result with $N = 5.5 \cdot 10^6$ meshcells. The simulation run with only $N = 1.9 \cdot 10^6$ meshcells is accurate within one percent for the resonance characteristics (resonance strength, frequency and linewidth) of both the main resonance as the smaller resonance around $\nu = 5.7 \cdot 10^{14}$ Hz as compared with the most accurate run.

The EB method is more expensive in terms of simulation runtime. Because the method is based on subsequent refinement of the mesh, several runs are necessary and the total cumulative solver times should be considered. The corresponding times for this mesh optimization can be found in table 4.2. Comparing these values with the ES method, it is clear that the EB method takes approximately twice as long, but the convergence is much better at a much lower amount of meshcells.

Simulation run	Meshcells [millions]	Cumulative solver time [min]
1	0.21	8
4	1.10	118
5	1.87	271
6	3.21	678
7	5.48	1340

Table 4.2: Simulation times during EB meshing optimization

4.2.2 Material description

For the description of material properties a material database is included in CST. However, the relevant parameters in the database, such as the electric permittivity ϵ or the magnetic permeability μ, are in most cases only given at the single radio frequency of 10 GHz. CST offers the possibility to add new metallic and dielectric materials to the database with user-defined characteristics, as long as the material behavior can be described by the following model.

To have a correct description of gold at optical frequencies, empirical data for the electric permittivity of gold from Johnson & Christy [17] is fitted to a general polynomial model

$$\epsilon(\omega) = \epsilon_\infty + \sum_{n=1}^{2} \frac{\gamma_{0,n} + i\omega\gamma_{1,n}}{\delta_{0,n} + i\omega\delta_{1,n} - \omega^2}. \tag{4.1}$$

Equation 4.1 describes a complex resonant model of 4th order, where ϵ_∞ is the electric permittivity at zero frequency (DC) and $\gamma_{\{1,2\},n}$ and $\delta_{\{1,2\},n}$ are fitting parameters which can be related to a physical interpretation in terms of poles and zeros by formulas 4.2 to 4.6

$$\omega_{pole,n} = \sqrt{\delta_{0,n}} \tag{4.2}$$

$$\omega_{zero,n} = \frac{\gamma_{0,n}}{\gamma_{1,n}} \tag{4.3}$$

$$Q_n = \frac{\sqrt{\delta_{0,n}}}{\delta_{1,n}} \tag{4.4}$$

$$G_n = \frac{\gamma_{0,n}}{\delta_{0,n}} \tag{4.5}$$

$$\tag{4.6}$$

where $\omega_{pole,n}$ is the angular frequency of the n-th pole, $\omega_{zero,n}$ is the angular frequency of the n-th zero, Q_n is the quality factor of the n-th pole and G_n is the partial strength or gain of the n-th pole. Using this model, the fitted values for the physical parameters are shown in table 4.3 and the empirical data and the fit are plotted in figure 4.4.

Parameter	Value
ϵ_∞	1 [F/m]
$\omega_{pole,1}$	$6.4224{\cdot}10^{14}$ rad$\cdot$s^{-1}
$\omega_{pole,2}$	$5.2096{\cdot}10^{13}$ rad$\cdot$s^{-1}
$\omega_{zero,1}$	$3.0206{\cdot}10^{14}$ rad$\cdot$s^{-1}
$\omega_{zero,2}$	$7.0612{\cdot}10^{15}$ rad$\cdot$s^{-1}
Q_1	1.2731
Q_2	3.4779
G_1	2.6616
G_2	1533.6

Table 4.3: Fitted parameter values for empirical data of the electric permittivity of gold

As can be seen from figure 4.4, the 4th order fit of the electric permittivity of gold corresponds sufficiently with the empirical data for wavelengths greater than 400 nanometer, which is the wavelength range of interest. Lower order models are not in sufficient agreement with the empirical data, because in that case either the low or high wavelength region is correctly described but not both. Higher order models could be used if the application demands a better correspondence with the empirical data, but this comes at a higher

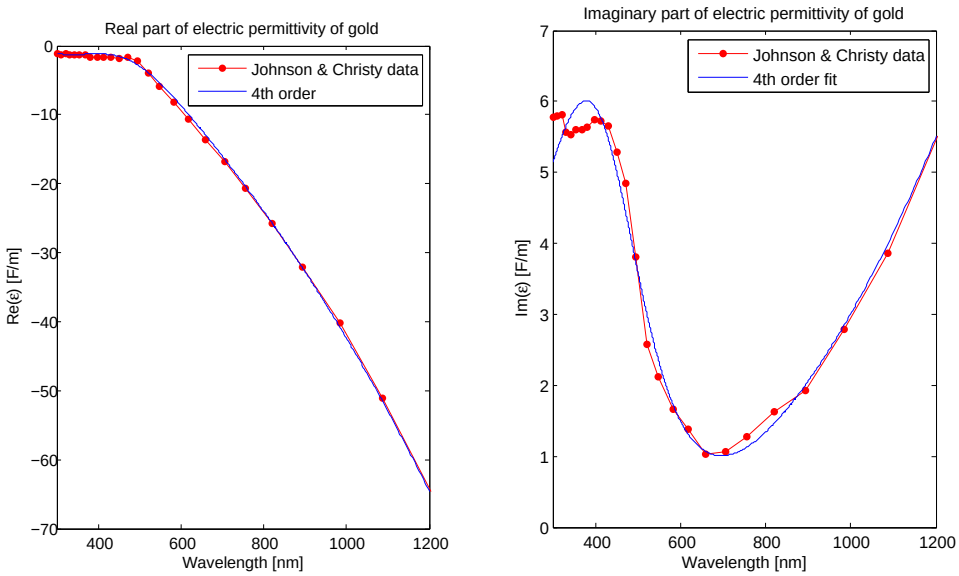

(a) Real part (b) Imaginary part

Figure 4.4: Electric permittivity ϵ of gold used in simulations

computational cost since for each order an extra differential equation has to be solved. Since the empirical data was obtained for thermally evaporated thin films of gold, the electric permittivity might differ from samples which are fabricated with differing methods. Therefore, within this project the accuracy of the model is sufficient, keeping in mind that the used electric permittivity for gold might differ when compared to experiments. The 4th order fit will be used in the following simulations.

4.2.3 Extraction of near-field data as function of time

To analyze the coupling of two structures, the near-field of both structures has to be compared. In CST only a few tools are available to extract simulated fields.

Far-field	Near-field
Extinction cross section	Time averaged field on curve
Scattering cross section	Time averaged field in volume
Absorption cross section	Time averaged field on plane
Directionality	Field in single point
Field in single point	

In the case of closed systems such as microresonators, CST has a build-in mode solver to find the eigenmodes of certain electromagnetic problem. How-

ever, for open systems such as nanoantennas, none of the build-in functions gives the local field as function of both location and time. The fields can only be shown as function of time, not as function of frequency (or incident wavelength) thus analysis of modal coupling of nanoantennas is not directly possible. An software extension to CST in the form of a VisualBasic macro was written to be able to extract the desired information. The extension generates a series of near-field time monitors at desired locations above the structures before the simulation starts and exports the data automatically when the simulation is finished. Afterwards the data is analyzed in Matlab.

The exported simulation data consists of the electric field 10 nanometers above the bar and ring structure, along the axis of the respective structure. Since the field is known as function of both position and time, the field as function as frequency or spatial frequency (k-vector) can be calculated used the Fourier transform.

$$\begin{array}{ccc} \vec{E}(x,t) & \xrightarrow{\mathbb{F}(x)} & \vec{E}(k,t) \\ {\scriptstyle \mathbb{F}(t)}\downarrow & & \downarrow{\scriptstyle \mathbb{F}(t)} \\ \vec{E}(x,\omega) & \xrightarrow[\mathbb{F}(x)]{} & \vec{E}(k,\omega) \end{array}$$

In this manner the coupling between the two structures can be investigated using only a single simulation run performed in CST. In case of the fields on the bar, the fields are transformed first into cylindrical coordinates and then Fourier transformed.

4.3 Simulations of gold nanostructures

With current top-down fabrication methods only nanostructures with straight edges can be fabricated reliably. Therefore the half wave nanoantenna and the nanoring simulated in this section have a rectangular cross section as opposed to a circular cross section as described in the theory. From literature it is expected that a different cross section has only a minor influence on the resonance conditions [11]. Because of fabrication limitations, the height of the structures is kept constant for most simulations at 30 nanometer. The gold will be described by the 4th order fit as described in section 4.2.2 and the material surrounding the antenna structures is taken to be vacuum. For meshing the EB method is used.

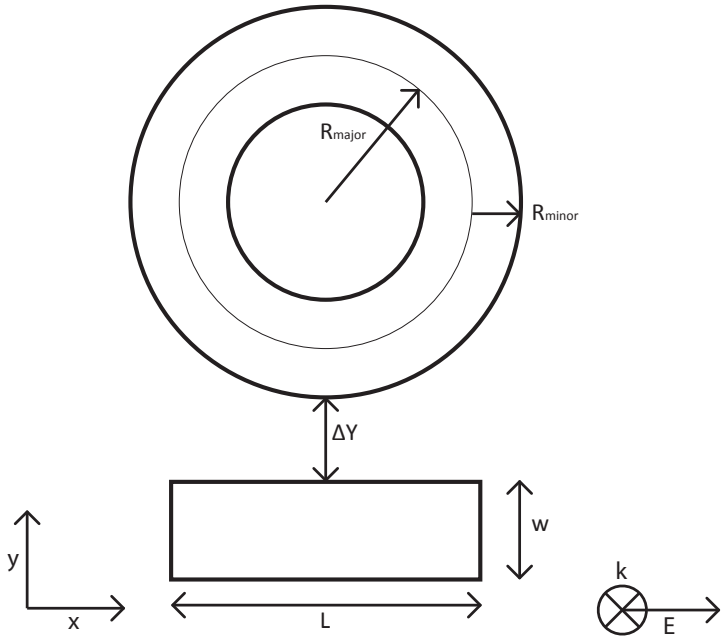

Figure 4.5: Geometry of simulated ring and bar structures as seen along z-axis. The structures have a height h in the z direction.

4.3.1 Optical response of single bar

A gold nanobar antenna of various geometries (length L, height h and width w) is simulated such that it can be compared with the optical wavelength scaling theory for antenna. A broadband pulsed planewave incident at normal angle and with the electric field vector aligned along the long axis is used as excitation source, so only dipole resonances can be excited in the structure. The local electric field is simulated and exported as described in section 4.2.3.

Influence of length

The width and height of the gold bar are kept constant at 30 nm. The length is varied between 20 and 220 nanometer. The maximum field energy $|E|^2$ as function of excitation wavelength is derived from the simulation data and shown in figure 4.6.

Since the local field and thus also the field energy assume a maximum at resonance, it is clear that the classical antenna law fails to describe the resonant length of the antenna as function of length. The smaller resonance seen around $\lambda = 600$ nm is probably due to a plasmon resonance along the short axis of the antenna.

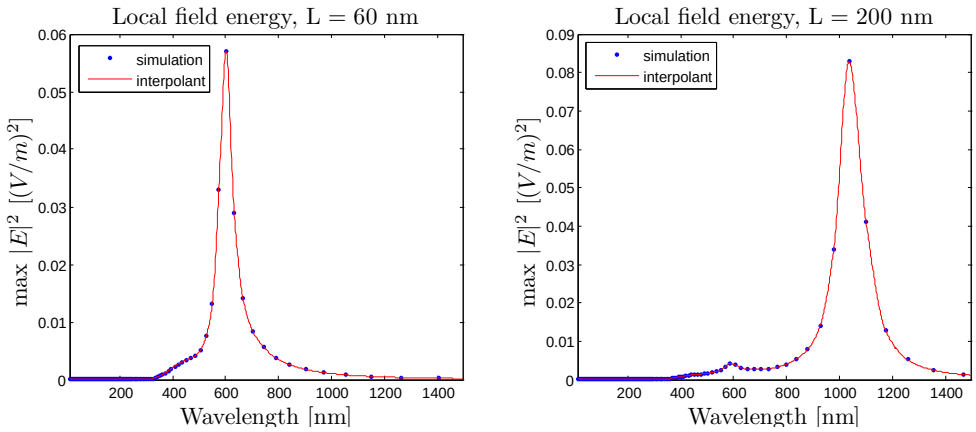

Figure 4.6: Simulated local field energy maxima as function of incident wavelength. Both the width and height of the gold bar is 30 nm

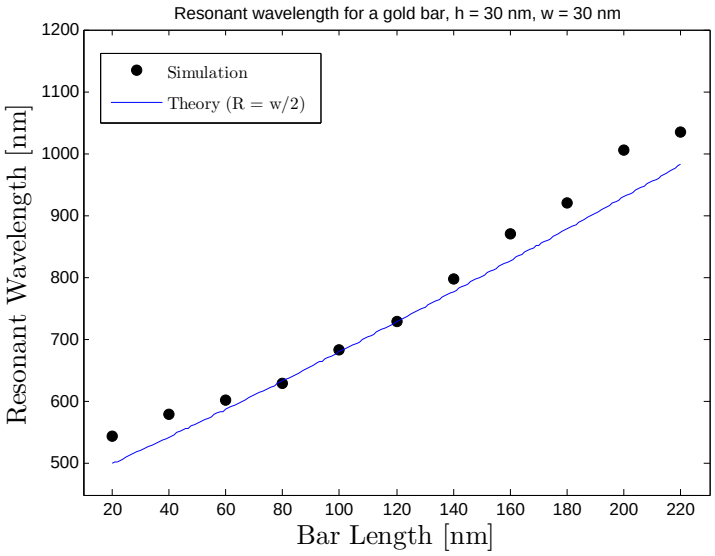

Figure 4.7: Simulated resonance wavelength as function of bar antenna length. Both the width and height of the gold bar is 30 nm

In figure 4.7 the simulated resonant wavelength of bar antennas of differing length is shown, along with the theoretical prediction using formula 3.3. It is assumed that the bar can be approximated as a cylinder with a corresponding cylindrical radius of $R = w/2$. The theory and the simulation data are in approximate agreement within 12 percent. Taken over the whole spectrum, the trend is fairly well predicted by theory.

Influence of the cross section

Using the same simulation parameters as above the influence of the width on the resonant wavelength is investigated. The length is fixed at 100 nanometer and the height at 30 nanometer.

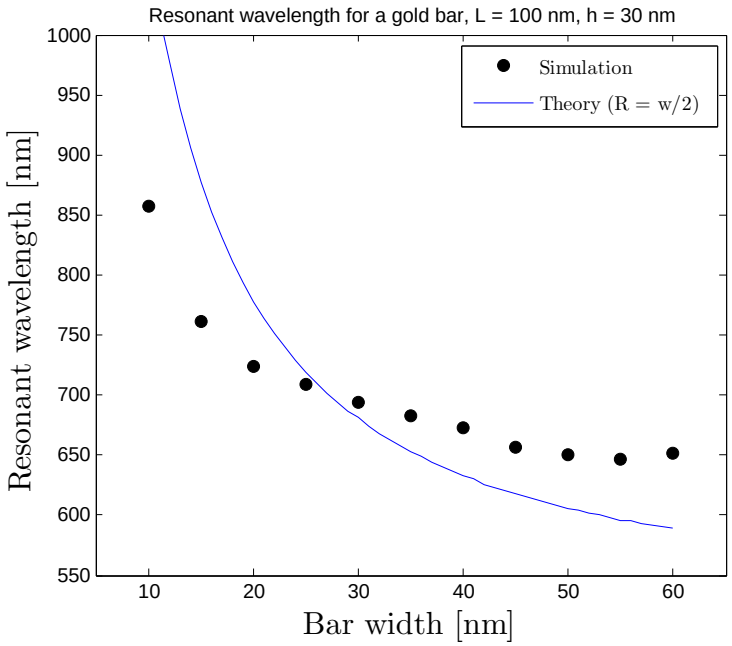

Figure 4.8: Simulated resonance wavelength as function of bar antenna width. The length is 100 nm and and the height is 30 nm

The results from the simulation are shown in figure 4.8. Although the resonance is clearly tunable by changing the width only, the assumption that the bar can accurately be described as a cylinder with radius $R = w/2$ clearly fails for a significant difference between the two short axis of the bar, e.g. a difference between the height and the width. A mismatch of 20 nanometer between the height and the width would cause a difference with the theoretical prediction by approximately 7%.

The same simulation is repeated as above, but now with the height and the width of the bar antenna linked such that the antenna has a symmetric cross section. The results are shown in figure 4.9. Figure 4.9 shows an excellent agreement between the theory and the simulation for small antennas with a width and height smaller than 35 nanometer. Thicker antennas deviate approximately 3 percent from theory, which could be explained by the fact that at larger cross sections the deviation of a cylinder becomes larger for which the theory is less correct.

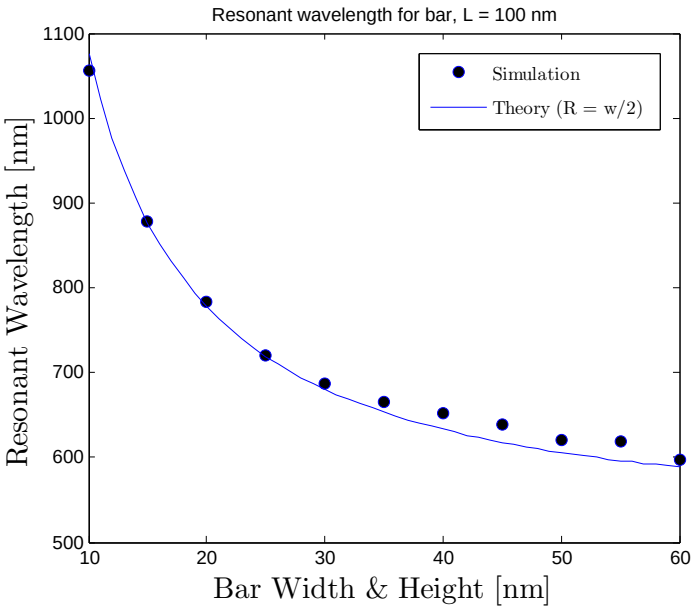

Figure 4.9: Simulated resonance wavelength as function of bar antenna width and height. The length is 100 nm.

4.3.2 Optical response of single ring

A gold nanoring antenna which consists of a short, hollow cylinder with a height h, a major radius R_{major} and minor radius R_{minor}, such that the inner diameter is $R_{major} - R_{minor}$ and the outer diameter is equal to $R_{major} + R_{minor}$, is simulated such that it can be compared with the optical wavelength scaling theory for antenna and with the bar antenna. The excitation planewave is incident under normal angle with the plane of the ring. The same simulation parameters and post-processing is applied as with the bar antenna. It is assumed that for a dipolar resonance the ring can be described like a standing plasmonic wave of plasmons on a infinite wire with radius R_{minor} (see section 3.2).

Excited ring modes

A gold nanoring with a minor radius of $R_{major} = 50$ nm, $R_{minor} = 24$ nm and a height of $h = 30$ nm is simulated and the electric field along the circumference of the ring $\vec{E}(s,t)$ is used to calculate the field as function of k-vector and frequency $\vec{E}(k,\omega)$ using the Fourier transform. The total local field energy $|\vec{E}(k,\omega)|^2$ is calculated and shown in figure 4.10 for the k-vectors corresponding to the dipole ($N = 1$) and quadrupole ($N = 2$) mode of the

ring. The scale is converted into wavelength for comparison.

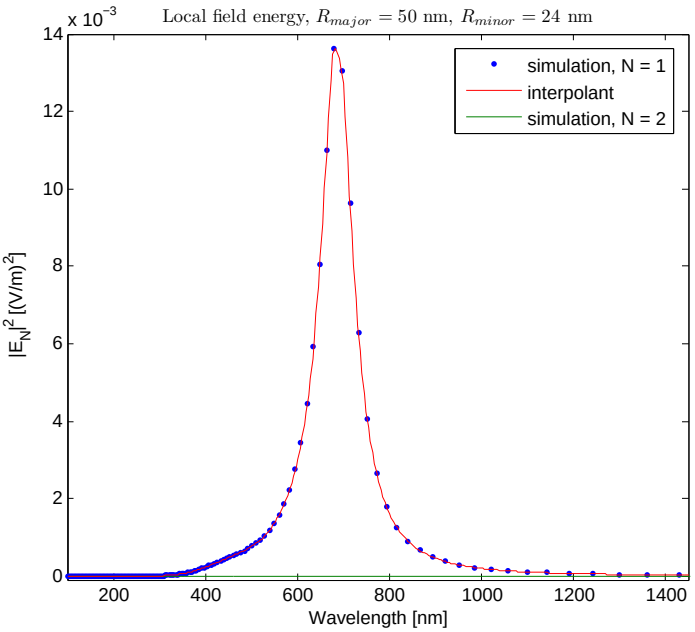

Figure 4.10: Local field energy for a single gold ring as function of wavelength for the dipole ($N = 1$) and quadrupole ($N = 2$) mode.

The simulation shows that only the dipole mode is excited under these excitation conditions. The higher order modes have a energy close to zero over the whole spectrum. This example is characteristic for the following simulations.

Influence of major radius

A gold nanoring with a minor radius of $R_{minor} = 10$ nm and a height of $h = 30$ nm is simulated while varying the major radius R_{major} from 20 to 70 nm. The corresponding resonance wavelength and the theoretical prediction using formula 3.3 are shown in figure 4.11.

The trend is in resonance wavelength as function of major radius is accurately predicted by the model only when the radius of the theorical waveguide (as described by formula 3.3) is taken to be $h/2 = 15$ nm instead of the actual $R_{minor} = 10$ nm. This shows that in case of a asymmetric cross section the choice of effective radius is not as clear as is the case with the nanobar antenna.

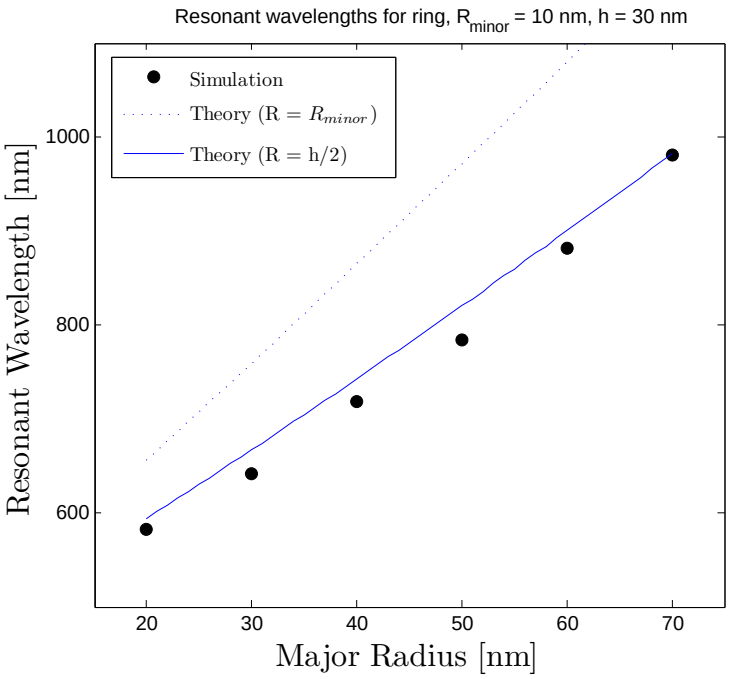

Figure 4.11: Simulated resonance wavelength as function of ring antenna major radius. The minor radius is 10 nm and the height is 30 nm.

Influence of minor radius

The same simulation is performed as in the previous section, but now varying the minor radius R_{minor} from 2 to 40 nm. The height is constant at 30 nm and the major radius is 50 nanometer.

As is seen in figure 4.12 the dependence on the minor radius is not accurately predicted by theory because of the asymmetry in the waveguide. For the symmetric case ($R_{minor} = 15$ nm), the difference with the simulation is approximately 10 percent.

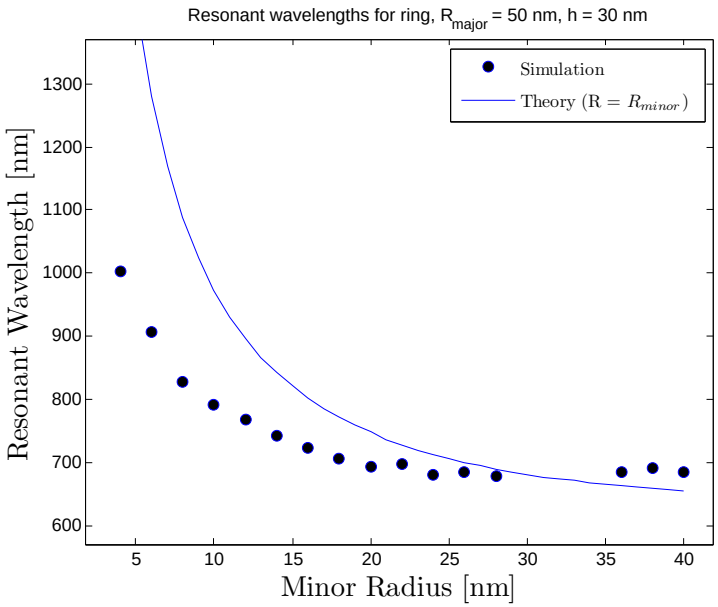

Figure 4.12: Simulated resonance wavelength as function of ring antenna minor radius. The major radius is 50 nm and the height is 30 nm.

4.3.3 Optical response of combined bar ring structure

A combined structure consisting of a bar with fixed dimensions $L = 88$ nm, $w = 50$ nm and $h = 30$ nm and a ring with fixed dimensions $R_{minor} = 25$ nm and $h = 30$ nm is simulated. The distance between the two structures ΔY is variable between 15, 30 or 50 nm and R_{major} is varied between 80 and 200 nm.

The maximum local field energy $\max |E_N(\omega)|^2$ for the first four ring modes ($N = 1..4$) above the ring as function of R_{major} is calculated from the simulation data as is shown in figure 4.13. Similar graphs for $\Delta Y = 30$ nm and $\Delta Y = 50$ nm are included in appendix A for better readability. For some data sets is was not possible to load the exported data due to data corruption. The problem has shown to occur precariously. While the exact origin of this problem is unknown, it has to be sought either in way CST parameterizes subsequent simulation runs or within the data-extraction extension.

Figure 4.13 shows that the dipole, quadrupole and hexapole mode can be excited depending on the major radius of the ring. The dipole mode becomes weaker as the radius becomes larger, as can also be seen in figures A.1 and A.2. This can be explained by a larger mismatch between the dipole mode on the bar and ring. The quadrupole and hexapole mode seem to couple optimally for $R_{major} \approx 100$ nm and $R_{major} \approx 150$ nm respectively, although the resolution does not allow to draw a conclusion solely based on those values. The same figure for $R_{major} = 97.5$ nm is placed in the appendix.

To have a clearer picture of the modal structure of the ring, the local field energy for the four modes on ring as function of excitation wavelength is shown in figure 4.14 for the case of $R_{major} = 150$ nm.

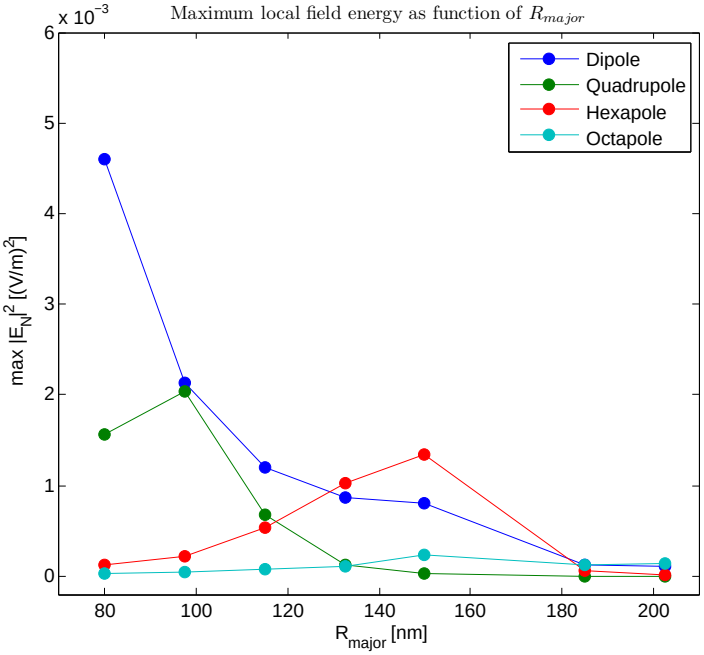

Figure 4.13: Maximum local field energy as function of R_{major} with $\Delta Y = 15$ nm.

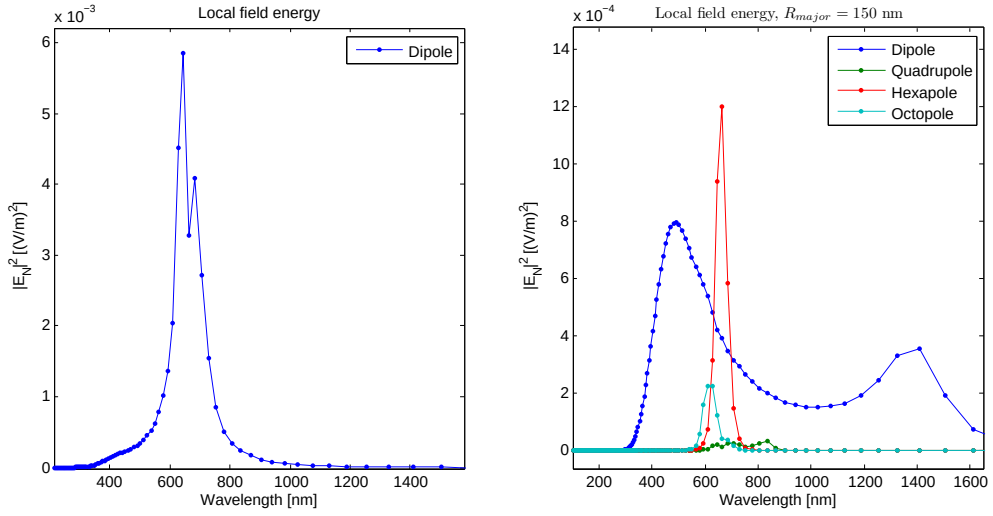

(a) Bar (b) Ring

Figure 4.14: Local field energy for the bas and ring modes for $R_{major} = 150$ nm as function of wavelength.

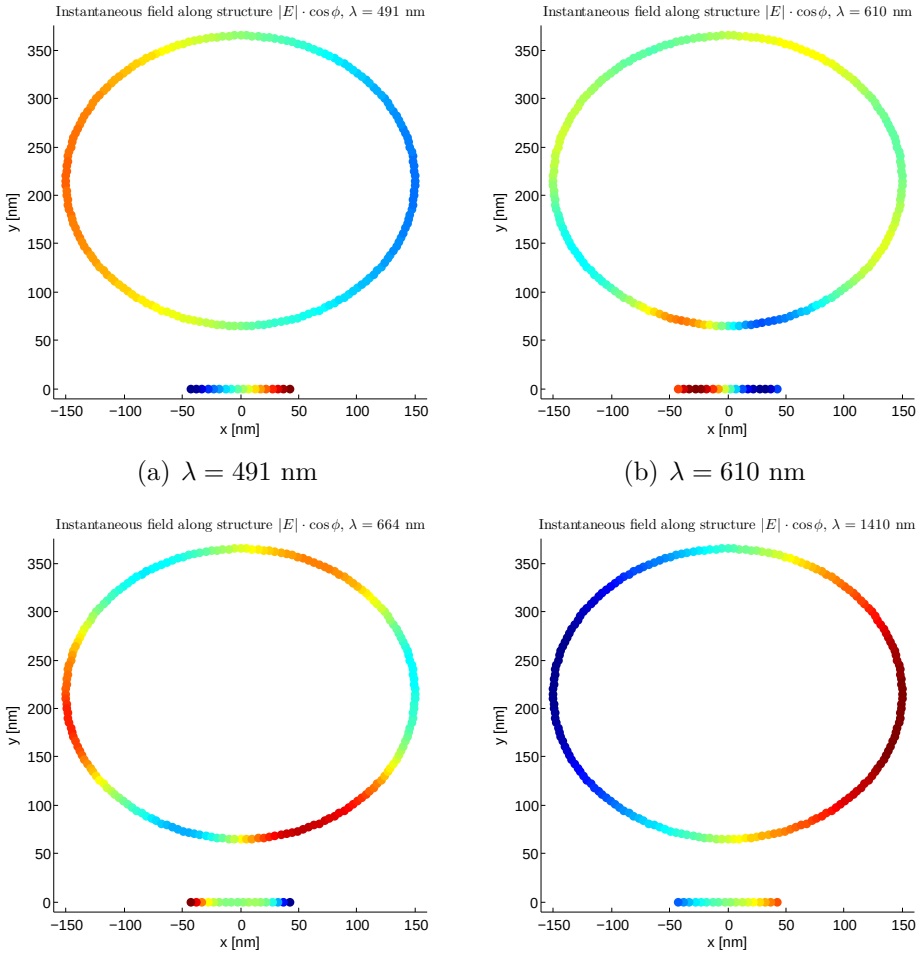

(a) $\lambda = 491$ nm

(b) $\lambda = 610$ nm

(c) $\lambda = 664$ nm

(d) $\lambda = 1410$ nm

Figure 4.15: Instantaneous field $|E| \cdot \cos(\phi)$ along structure for several wavelengths for structure with $\Delta Y = 15$ nm and $R_{major} = 150$ nm.

The corresponding field energy is included for the bar as well. A narrow hexapole mode (FWHM ≈ 50 nm) is clearly visible around $\lambda = 664$ nm. Also the splitted dipole mode is visible around $\lambda = 491$ nm and $\lambda = 1410$ nm. A small quadrupole mode is visible around $\lambda = 610$ nm. The corresponding instantaneous electric fields $|E| \cdot \cos(\phi)$ along the structure are shown in figure 4.15. ϕ is the spectral phase of the field and can be used to show that two structures resonating at the same frequency are either in phase or out of phase. This can be seen in the case of two dipole fields: the fields at $\lambda = 1410$ nm are in phase and represent a bonding mode. The dipole mode at $\lambda = 491$ nm is in anti-phase with the dipole mode on the bar and represents a so called anti-bonding mode. Since the oscillating charges are closer together,

the restoring Coulomb repulsion force is larger and the oscillation occurs at a higher frequency in case of the anti-bonding mode as opposed to the bonding mode which oscillates at a lower frequency (with a corresponding larger wavelength). The nomenclature for these bonding modes is taken from molecular physics: when two atoms bond together to form a molecule, the resulting wavefunction for the electron density can have two different energies: one with a higher energy such that the atoms are repulsed (anti-bonding) and one with a lower energy such that binding occurs.

The resonance wavelength and FWHM linewidth of all found simulated dipolar bar resonances and non-dipolar ring resonances are registered in table A.1 to A.3 in appendix A. In figure 4.16 a comparison is made between all ring modes and theory. The theory predicts the resonant wavelengths within 7% for the higher order ring modes with R_{major} ranging from 80 to 200 nanometer and a R_{minor} of 25 nm.

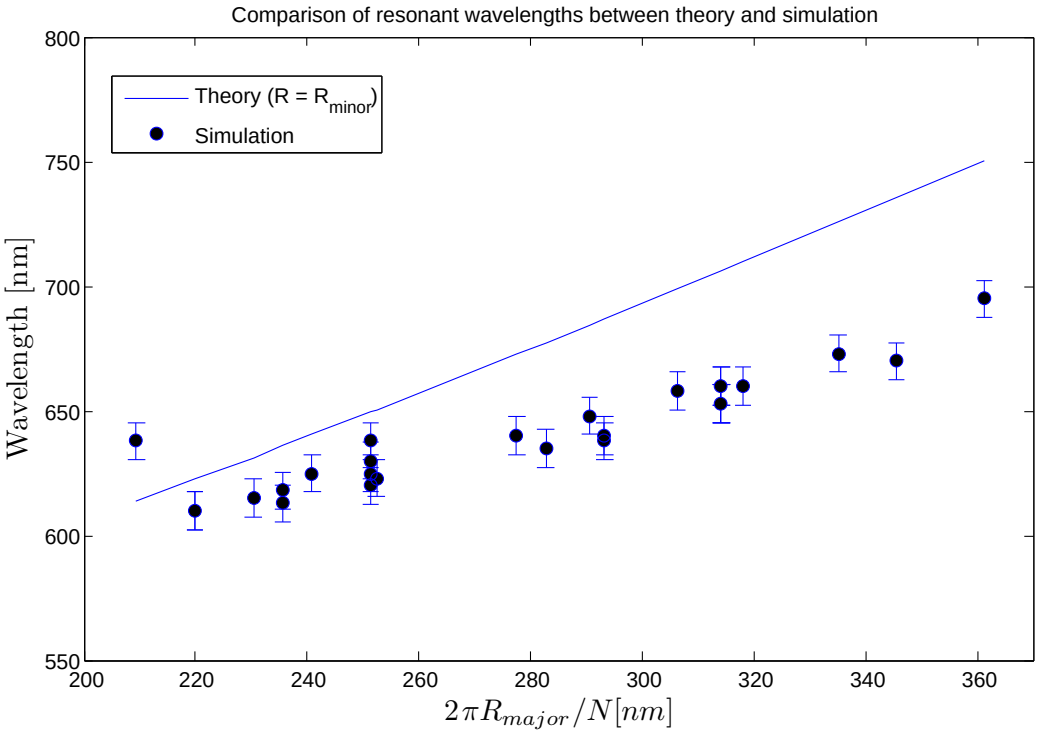

Figure 4.16: Comparison of theory and simulation for resonant wavelength

The average linewidth found for the higher order ring modes for the strongest coupled case ($\Delta Y = 15$ nm) is 58 ± 5 nm. The corresponding average of the bar mode is equal to 71 ± 6 nm so the coupling to a higher order ring mode can increase the lifetime by a small amount. However, fabri-

cation imperfections will most probably cancel the marginal advantage. The same holds for the other two cases.

4.4 Conclusion and discussion

Simulations on a single bar, a single ring and coupled bar and ring antenna structures have been performed. It is found that a linear scaling law, accounting for plasmonic effects in nanoantennas, can be used to predict the resonance wavelengths based on classical resonance conditions for a bar and ring antenna for large scale antennas. The theory is typically accurate within 10%, depending on the geometry.

Coupling of the dipole mode to higher order ring modes is possible for narrow wavelength ranges (typically 50 nm) but no apparent gain in oscillation lifetime has been observed. Since the dipole and higher order mode are coherently coupled, it would not be possible to store energy in the 'non-radiative' higher order mode because it is tightly coupled to a radiative mode. A possible solution would be to use a chain of rings to carry the energy away from the dipole mode. For this to work an efficient ring-ring coupling must exist for the incident wavelength and the intrinsic material loss should be sufficiently low. The results shown here provides the first step for such sub-wavelength waveguide.

In a few cases the exported data was corrupted, but this might indicate a problem in the simulation in CST itself. Except from that, the near-field extension for CST works as expected and gives direct access to near field information. This method provides the user with a lot of freedom and is thus a powerful add-on to CST.

Chapter 5

Fabrication of gold nanostructures

5.1 Introduction

For the realization of plasmonic nanostructures several techniques are available. The two most frequently used techniques are focused ion beam milling (FIB) and e-beam lithography. In this work FIB was chosen because of the required resolution, the availability of in-house knowledge. The actual fabrication was performed using the excellent infrastructure at the MESA+ institute of nanotechnology.

5.2 Gold thin films

Two methods of gold thin film fabrication have been used.

5.2.1 Poly crystalline gold films using sputtering

A thin gold film of 30 nanometer is deposited on a substrate using thermal sputtering of gold. As a substrate both glass as glass with a thin layer of indium tin oxide is used. The physical vapor deposition method (PVD) yields a controllable thickness with an accuracy better than 5 nanometer. The produced gold films are typically poly cystalline with a grain size of 10 to 30 nanometer.

This method has several advantages.

1. The thin film area usable for following production steps is large (multiple square centimeters).

2. Film thickness is well controlled and can be chosen within 5 nanometer accuracy. No additional fabrication steps are needed to adjust the thickness afterwards.

3. It consists of a single fabrication step.

The disadvantage of the PCD method is the roughness of the thin film due to the grains, which is the limiting factor when high resolution (20 nm) structures are desired.

5.2.2 Mono crystalline gold films using chemically grown flakes

In the recent years new methods have become available to synthesize all kinds of gold nanoparticles with controllable shapes and good monodispersity [18]. In a recent paper, Huang et al. developed a chemical synthesis (CS) process to synthesize atomically flat, single crystalline gold crystals [19]. This methods was implemented together with D.J. Dikken M.Sc. of the Optical Sciences group.

Depending on the synthesis parameters such as temperature, timing and concentrations, not only single crystals but a variety of nanoparticle shapes grow. The single crystals are usually not monodisperse and thickness typically vary between 50 and 300 nanometer, while the area varies between 500 and 10.000 square micrometers with the tendency that thicker crystals are larger.

After synthesis the solution with flakes and other particles is flown over a glass or glass with ITO substrate and blown dry. The adhered particles are observed using a optical microscope and the thinnest, single crystalline particles are selected. The selection is based on the characteristic shape and the fact that flakes with a thickness smaller than 200 nm are partially transparent.

In case of a glass substrate, a carbon sticker is placed placed close to the flakes and a conducting wire is deposited from the carbon to the flake using FIB-assisted chemical vapor deposition. This is necessary because a grounded sample is needed for FIB to prevent local changing. These steps are not needed in case of a ITO substrate because ITO conducts sufficiently.

The gold flake is thinned by a a single milling step. If the desired thickness is achieved a pattern can be carved out of the gold using FIB milling.

5.3 Milling strategies

Milling of thin gold films is known to be hindered by a few difficulties.

1. The milling speed is much higher at slopes. This implicates that when the thin film is not smooth, milling enhances (amplifies) the unwanted surface roughness.

2. Gold redeposition from milled areas causes unwanted asymmetry in the resulting structures when milling in a raster-like manner.

3. The milling speed is thermally sensitive with respect to the used substrate. Therefore a calibration for each substrate must be made.

To fabricate gold nanostructures using FIB milling with typical smallest feature sizes of ten to twenty nanometers, a smart milling sequence has to be employed. For each structure a specialized structure definition file is generated, containing a specific sequence and dwell time which which the focused ion beam is directly controlled. In this work these so called 'stream files' are generated with a Matlab script and can be loaded into the control software of the FEI NovaLab600 dual-beam machine. The FIB process was operated by and optimized with the help of ing. F.B. Segerink of the Optical Sciences group. The basic design rules are: large surfaces first, mill from different directions alternately and mill the smallest features (such as gaps) lastly. An example is shown if figure 5.1.

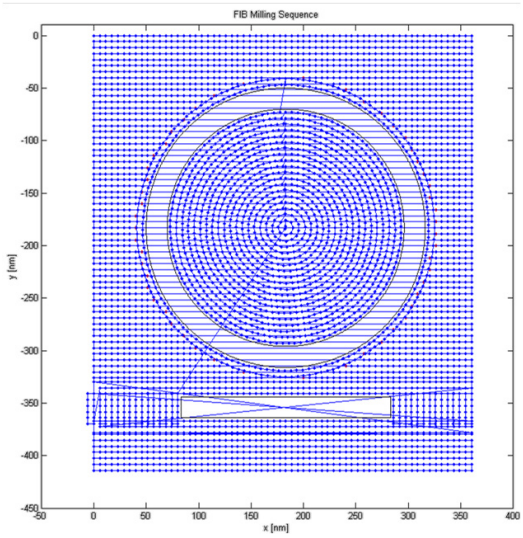

Figure 5.1: Example of a smart milling sequence for a bar ring structure.

5.4 Fabrication results

5.4.1 Poly crystalline gold

Nanobars with a length of 100 nanometer are fabricated using FIB milling and a poly crystalline gold film.

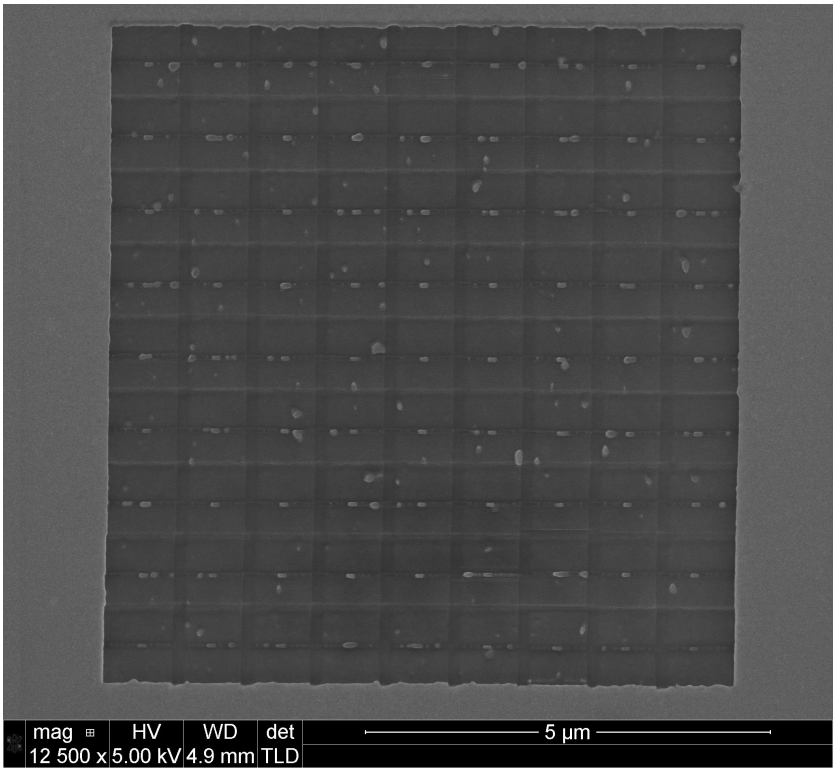

Figure 5.2: SEM micrograph of FIB fabricated nanoantennas on poly crystalline gold, overview.

As can be seen in figure 5.3, the roughness of the initial thin film has been converted into small gold islands. Although nanoantennas with a desired length of 100 nanometer are fabricated, the gold islands are clearly obstructing the desired pattern.

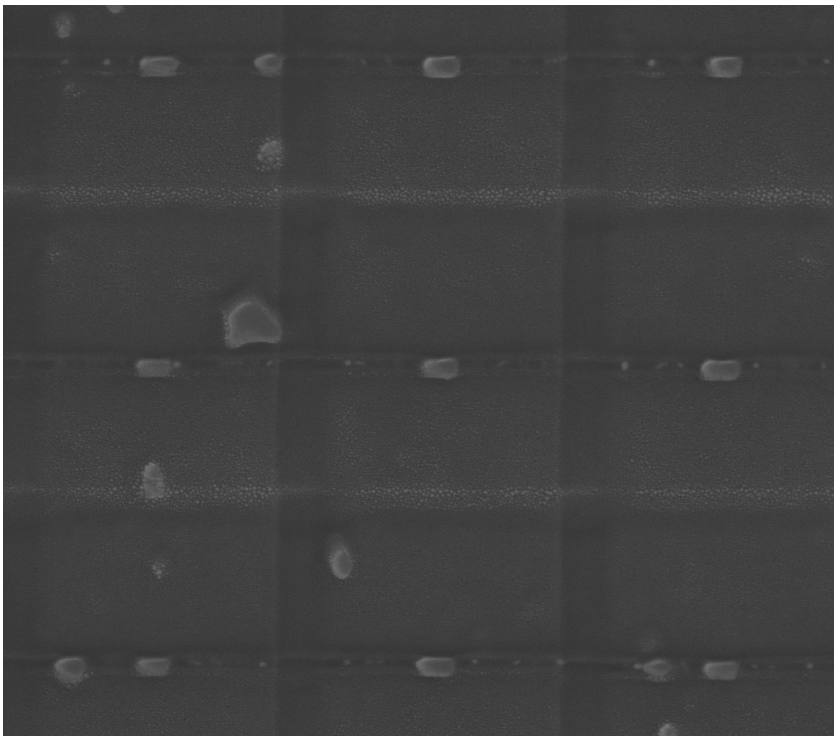

Figure 5.3: SEM micrograph of FIB fabricated nanoantennas on poly crystalline gold, zoom. The window width is 2.5 μm.

5.4.2 Single crystalline gold

The same pattern as in the previous case was milled into a single crystalline gold flake. The results are shown in figure 5.4 and 5.5.

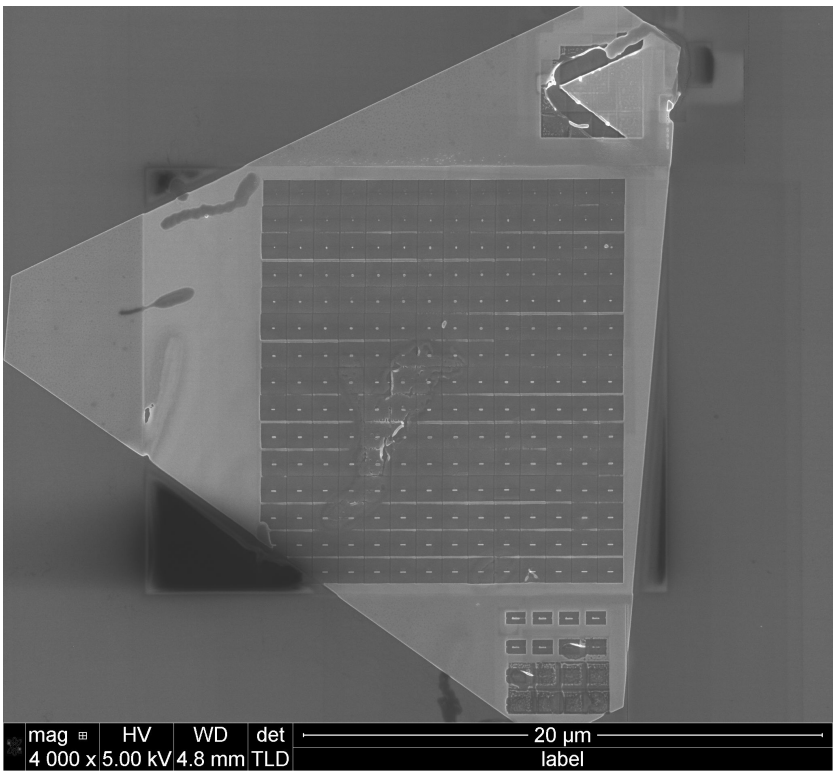

Figure 5.4: SEM micrograph of FIB fabricated nanoantennas on single crystalline gold, overview.

As apparent from figure 5.4, some organic material is contaminating the flake. The effect of such contamination is clearly visible in figure 5.5. The pattern is locally disfigured, but outside the contaminated area the bars are of excellent quality. The fabrication reproducibility of these antennas is approximately 5 nanometer. The problem of contamination should be countered from two sides: optimize the synthesis procedure such that less organic material is present in the solution and/or look for a different flake with less contamination. The FIB thinning step does not significantly increase the surface roughness.

Another fabrication example is shown in figure 5.4.2. The ring are slightly asymmetric, but reproduce very well. The bar length is 100 nm, the ring wall alternates between 30 and 35 nm and the gap size is less than 20 nanometers.

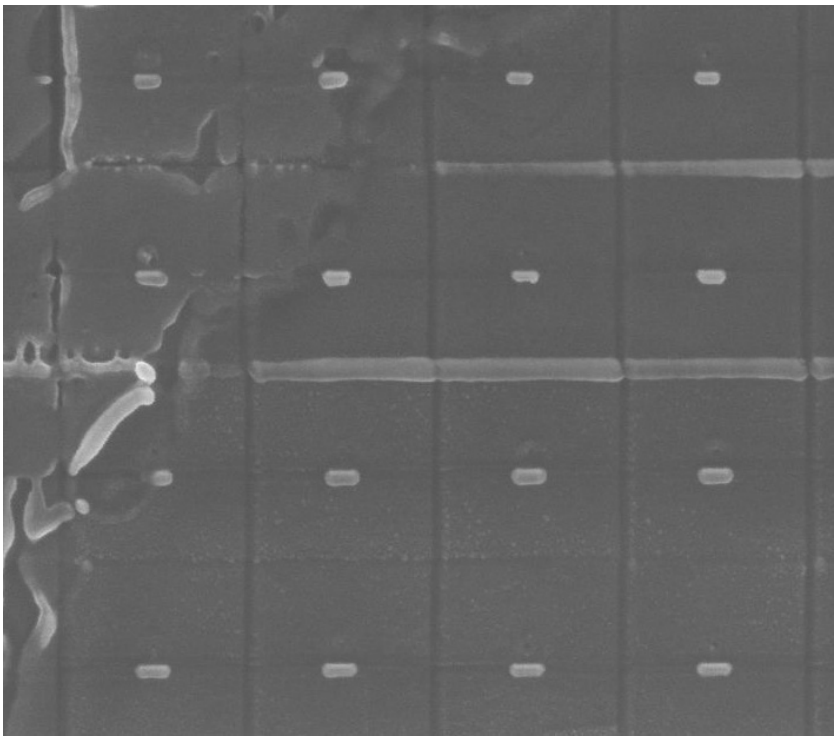

Figure 5.5: SEM micrograph of FIB fabricated nanoantennas on a single crystalline gold flake. The window width is 2.5 μm.

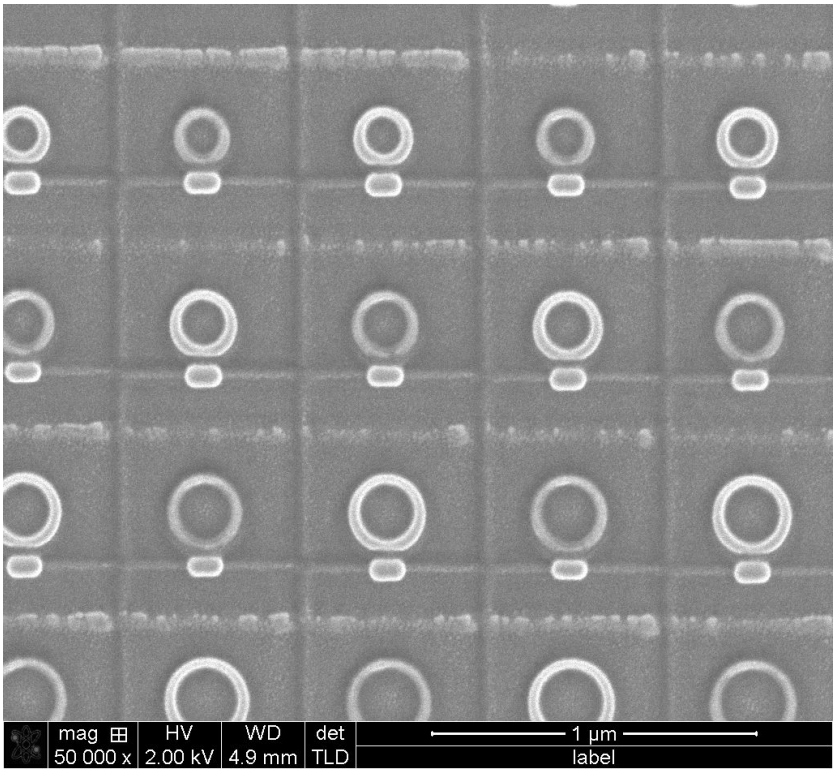

Figure 5.6: SEM micrograph of FIB fabricated bar ring structures on a single crystalline gold flake.

5.5 Conclusion

The use of single crystalline gold flakes is advantageous when small feature sizes (20 nm) and a high reproducibility are needed. The use of a ITO substrate circumvents the need for grounding the small crystals using carbon stickers or FIB-assisted deposition of small metal wires.

Chapter 6

Spectroscopy of single nanoantennas

To measure the scattering properties of single nanoantenna, an optical setup was designed and build. The design requirements are as follows.

1. Broadband (visible and NIR spectrum)
2. Sensitive for the signal of a single nanoantenna
3. Accurate positioning of the sample
4. Partially automated to aid the measurement of multiple antenna

6.1 Experimental considerations

The strength of a scatterer can be given in terms of it's scattering cross section σ_{sca} $[m^2]$. The scattering cross section is hypothetical area which describes the chance that incident light is being scattered from the particle and is in general different than the geometrical cross section of the particle. The scattering cross section is part of the extinction cross section σ_{ext} $[m^2]$of a particle:

$$\sigma_{ext} = \sigma_{abs} + \sigma_{sca} \tag{6.1}$$

with σ_{abs} being the absorption cross section. The extinction cross section is related to the absorbance of a medium through the law of Lamber-Beer:

$$I(l) = 10^{-C \cdot l \cdot \sigma_{ext}} \cdot I_0 \tag{6.2}$$

with I_0 the incident irradiance, C the concentration of particles, l the length of the path traversed through the medium and $I(l)$ the resulting irradiance.

For a single particle of cross section σ_{ext} and a incoming light beam with area A_{beam}, the fraction of power which is scattered is

$$I_{sca} = \frac{\sigma_{sca}}{A_{beam}} \cdot I_0. \tag{6.3}$$

For a single cylindrical bar antenna of length $L = 100$ nm and diameter D =30 nm a typical scattering cross section of $\sigma_{sca} = 1 \cdot 10^{-14}\ m^2$ is found through FDTD simulations and in literature [8].

6.2 Setup

A crossed polarizers confocal scanning microscope has been chosen as the best solution. Confocality suppress signal from other locations than the antenna and the crossed polarizers suppress the non scattered signal sufficiently. Another option which has been considered intensively is the dark-field method, where light is collected at different angles than the angles at which the incident light illuminates the sample. This method might be successful when the dark-field signal is collected at the same side of the sample (by the use of a special objective) but in transmission mode scattering from the rest of the sample prevents decent filtering. A confocal pinhole to sufficiently shield from the scattering rejects too much signal, such that alignment of the dark-field field stop is not possible. Using a high power source might circumvent this problem.

A broadband lamp (Apex Arc High Stability Lamp Source, Xe) in combination with computer controllable 4f-monochromator is used to generate a selectable output wavelength between 500 and 1000 nm with a bandwidth of 8 nm over the whole spectrum. The 4f monochromator consists of a blazed, ruled grating (1200 lines per mm) which is mounted on a stepper motor with an stepsize of 1/100 degree. A lens (f = 125 mm) placed at f from the grating focuses the color component of a adjustable slit, which is adjusted to said bandwidth. Another lens (f = 125 mm) collimates the monochromatic light from the slit towards the sample stage.

A unused portion of the beam is diverted used a D-shaped mirror towards a 50:50 beam splitter, which divides the light between a photodiode (PIN 10D) and a 10x objective which focuses the light into a fiber for the fiber spectrometer (Avantes AvaSpec-3648). This part can be used to characterize the beam in terms of spectrum and power.

The total output spectrum of the light source is shown in figure 6.1. The data from the spectrometer was calibrated using a Spectra Physics 404 Optical power meter.

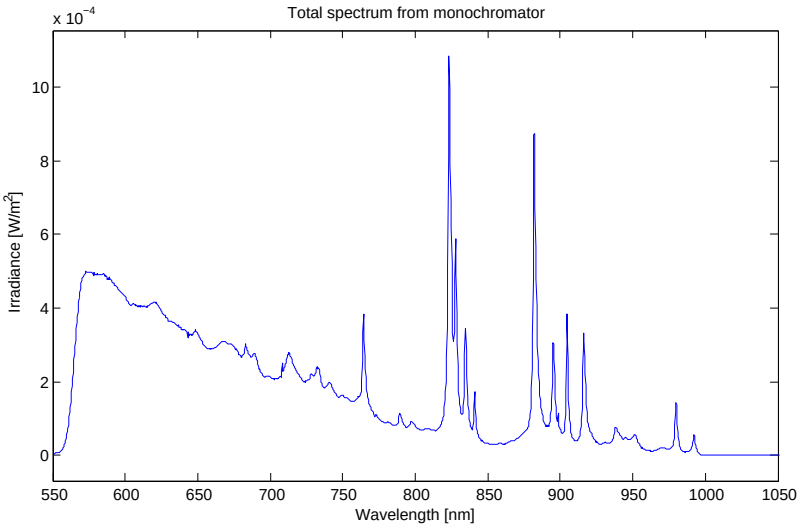

Figure 6.1: Total output spectrum from monochromator

Two broadband polarizers (Thorlabs Linear Film Polarizer LPVIS) in crossed configuration are used to suppress the non-scattered light. One is placed just before the sample stage, with the transmission axis rotated +45 degrees compared the the vertical axis, while the other one is placed just after the sample stage with the transmission axis rotated -45 degrees compared the the vertical axis. Light which traverses the sample stage without a change in it's polarization is reduced by a factor of 10^6 in the wavelength range of 550 to 1000 nm.

The sample stage consists of a excitation objective (Nikon M-Plan 40x 0.5 ELWD) which focuses the light down to a spot of approximately 40 by 40 μm through the substrate of the sample. The sample itself is mounted into a homemade sample holder made out of stainless ferromagnetic steel, such that samples can be secured using strong magnets. The sample holder is mounted on top of a SmarAct MSC x,y,z-nanopositioner which a maximum range of tens of millimeters and a positioning accuracy around 1 nm. The SmarAct has a build in feedback loop to compensate for drift.

A collection objective (Zeiss Plan Neo Fluar 0.75 NA ∞/0.17) collects the light directly from the samples surface. An achromatic doublet lens (f = 120 mm) is used as tubelens to focus the image through the secondary polarizer onto a 20 μm pinhole placed in front of a APD detector (EG&G SPCM-AQ-160). A flippable mirror can be used to divert the image onto a CCD camera to aid positioning.

The combination of the infinity corrected objective and the tube lens with f = 120 mm has a magnification of 24x. In combination with the used pinhole,

an area of approximately 830 nm in diameter in the focal plane is collected. This is suitable for both single structures as larger, combined structures. The sensitivity of the setup is limited by the extinction of the crossed polarizers. A count rate of approximately $3 \cdot 10^5$ counts per second (5% of maximum countrate) is due to non-filtered excitation light. The background light (from environment) is approximately 300 counts per second.

6.2.1 Control and data acquisition

The stepper motor and nanopositioner are controlled by the setup PC. A Labview program was written to perform raster scans with a user settable range and step size. At each position the monochromator is stepped through the whole spectrum. For each step the APD and photodiode are simultaneously read out, using a break-out board connected to a NI M-series DAQ card, so that a correction for fluctuating power from the lamp can be made. For each position the exact position is read out from the nanopositioner. If desired, also the full spectrum can be captured during each monochromator step.

6.3 Measurement results

The transmission of the sample is calculated using a reference measurement on an empty part of the sample, e.g. only glass. The transmission of the sample as function of wavelength is calculated as follows:

$$T(\lambda) = \frac{\frac{I_s}{I_{sp}}}{\frac{I_r}{I_{rp}}} = \frac{I_s(\lambda) \cdot I_{rp}(\lambda)}{I_r(\lambda) \cdot I_{sp}(\lambda)} \tag{6.4}$$

with I_s the measured signal from the APD, I_sp the measured signal from the PD, I_r the measured signal from the APD for the reference location and I_rp the measured signal from the PD for the reference location.

The sample consists out of small nanobars with a length of 100 nm and a width of 30 nm as seen in figure 5.4 and 5.5. The sample is placed such that the bars are vertical.

Two typical measured spectra are shown in figure 6.3 and 6.3.

As can be seen in the figures, no clear signature of the nanoantenna can be seen and strange artifacts can be seen for higher wavelengths. This has several causes.

1. The spectrum from the lamp is not smooth enough to approximate the monochromatic light as being a Gaussian, which is the basis of the

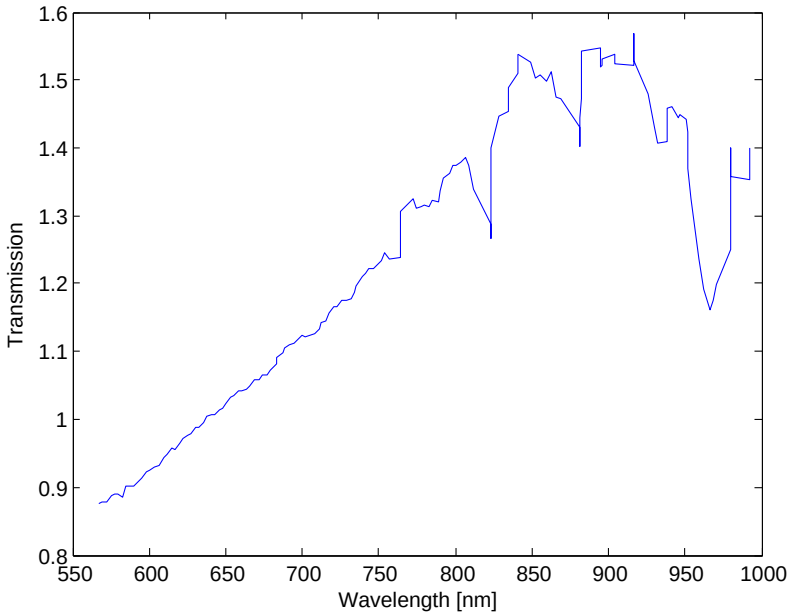

Figure 6.2: Typical measured transmission spectrum.

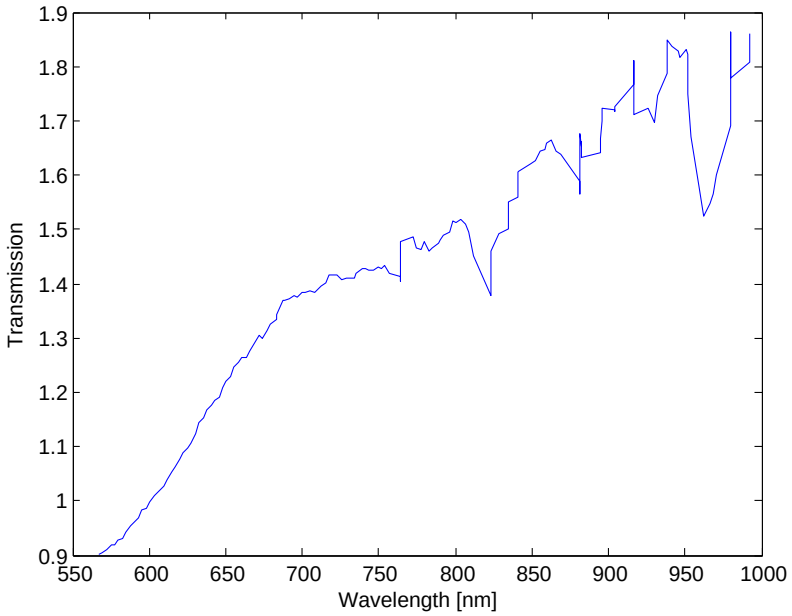

Figure 6.3: Typical measured transmission spectrum.

conversion between the steps of the stepper motor and wavelength.

2. The fabricated sample suffers from both organic residue and remaining gold between the antennas due to drift during the FIB milling.

The transmission is mostly above one, as would be expected with the crossed polarizer scheme. The large gold structures appear as very broad scatters in the spectrum and no clear signature of a antenna can be distinguished.

6.4 Conclusion and discussion

Due to an unsuitable sample and complicating spectrum from the broadband lamp no spectrum a single nanoantenna has been observed yet. The problem with the lamp spectrum could be compensated for if the spectrum at each stepper motor step n is measured. The measured intensity on the APD is proportional to

$$I_s(n) \propto \int S(\lambda, n) \cdot T(\lambda) d\lambda \tag{6.5}$$

with T the transmission of the sample and S(λ) the spectrum during measurement n. If a whole sequential measurement series is performed and the problem is discretized (sum over all λ)

$$I_s(n) \propto \sum S(\lambda, n) \cdot T(\lambda) \tag{6.6}$$

becomes

$$\vec{I_s} \propto \mathbf{S}(\lambda, n) \cdot \vec{T}(\lambda) \tag{6.7}$$

which is a normal linear algebra problem which might be solved for T(λ) if formula 6.7 is well conditioned. This idea has been explored shortly but preliminary results indicate that the spectrum varies too strongly such that no solution can found. The use of a highly sensitive spectrometer instead of this lamp combined with a monochromator would be a solution. Another solution would be to use different lamp with a smoother spectrum.

The fabrication of the nanoantenna is already adjusted to prevent the gold residue by a adjustment of the smart milling, but due to lack of time these samples could not be fabricated and measured in time.

Chapter 7

Discussion and Conclusions

Simulations on a single bar, a single ring and coupled bar and ring antenna structures have been performed. It is found that a linear scaling law, accounting for plasmonic effects in nanoantennas, can be used to predict the resonance wavelengths based on classical resonance conditions for a bar and ring antenna for large scale antennas. The theory is typically accurate within 10%, depending on the geometry.

Coupling of the dipole mode to higher order ring modes is possible for narrow wavelength ranges (typically 50 nm) but no apparent gain in oscillation lifetime has been observed. Since the dipole and higher order mode are coherently coupled, it would not be possible to store energy in the 'non-radiative' higher order mode because it is tightly coupled to a radiative mode. A possible solution would be to use a chain of rings to carry the energy away from the dipole mode. For this to work an efficient ring-ring coupling must exist for the incident wavelength and the intrinsic material loss should be sufficiently low. The results shown here provides the first step for such sub-wavelength waveguide.

In a few cases the exported data was corrupted, but this might indicate a problem in the simulation in CST itself. Except from that, the near-field extension for CST works as expected and gives direct access to near field information. This method provides the user with a lot of freedom and is thus a powerful add-on to CST.

The fabrication of the nanostructures using single crystalline gold flakes has been explored and the preliminary results are satisfying. Improvements can still be made, as the solution in which the flakes are conceived is not free from organic residue, which influences both fabrication and measurements in a negative manner. Also a large fraction of the produces flakes are too thick, which can be optimized by tuning the synthesis parameters. However, the low surface roughness and the absence of grains have pushed the possibilities

of nanostructure fabrication using of FIB milling further and are an attractive alternative to the physical vapor method.

No scattering spectra of single nanoantenna have been observed yet due to the influence of residue and fabrication artifacts, which is the limiting factor at the moment. The fabrication method has already adjusted to prevent the influence of drift during the FIB process on the fabricated samples.

Bibliography

[1] Michael Faraday. The bakerian lecture: On the relations of gold and other metals to light. *Proceedings of the Royal Society of London*, 8:356–361, 1856. ArticleType: research-article / Full publication date: 1856 - 1857 / Copyright 1856 The Royal Society.

[2] Naomi J. Halas. Plasmonics: An emerging field fostered by nano letters. *Nano Letters*, 10(10):3816–3822, October 2010.

[3] Lukas Novotny and Niek van Hulst. Antennas for light. *Nat Photon*, 5(2):83–90, February 2011.

[4] P. Muehlschlegel, H.-J. Eisler, O. J. F. Martin, B. Hecht, and D. W. Pohl. Resonant optical antennas. *Science*, 308(5728):1607 –1609, June 2005.

[5] Petru Ghenuche, Sudhir Cherukulappurath, Tim H. Taminiau, Niek F. van Hulst, and Romain Quidant. Spectroscopic mode mapping of resonant plasmon nanoantennas. *Physical Review Letters*, 101(11):116805, 2008.

[6] T. Kalkbrenner, U. Hakanson, A. Schaedle, S. Burger, C. Henkel, and V. Sandoghdar. Optical microscopy via spectral modifications of a nanoantenna. *Physical Review Letters*, 95(20):200801, November 2005.

[7] Lukas Novotny. Effective wavelength scaling for optical antennas. *Physical Review Letters*, 98(26):266802, June 2007.

[8] U Kreibig and M Vollmer. *Optical properties of metal clusters*. Springer-Verlag, 1995.

[9] C. Soennichsen, T. Franzl, T. Wilk, G. Von Plessen, J. Feldmann, O. Wilson, and P. Mulvaney. Drastic reduction of plasmon damping in gold nanorods. *Physical Review Letters*, 88(7):774021–774024, 2002.

[10] M. Quinten, A. Leitner, J. R. Krenn, and F. R. Aussenegg. Electromagnetic energy transport via linear chains of silver nanoparticles. *Optics Letters*, 23(17):1331–1333, 1998.

[11] Peter Nordlander. The ring: A leitmotif in plasmonics. *ACS Nano*, 3(3):488–492, March 2009.

[12] Heinz Raether. *Excitation of plasmons and interband transitions by electrons*. Springer, 1980.

[13] Chizuko M. Dutta, Tamer A. Ali, Daniel W. Brandl, Tae-Ho Park, and Peter Nordlander. Plasmonic properties of a metallic torus. *The Journal of Chemical Physics*, 129(8):084706, 2008.

[14] H. Devoe. Optical properties of molecular aggregates. i. classical model of electronic absorption and refraction. *The Journal of Chemical Physics*, 41(2):393–400, 1964.

[15] Kane Yee. Numerical solution of initial boundary value problems involving maxwell's equations in isotropic media. *IEEE Transactions on Antennas and Propagation*, 14(3):302–307, May 1966.

[16] Steven Johnson. Yee-cube. http://commons.wikimedia.org/wiki/File:Yee-cube.svg, September 2011.

[17] P. B. Johnson and R. W. Christy. Optical constants of the noble metals. *Physical Review B*, 6(12):4370, December 1972.

[18] Marie-Christine Daniel and Didier Astruc. Gold nanoparticles: Assembly, supramolecular chemistry, Quantum-Size-Related properties, and applications toward biology, catalysis, and nanotechnology. *Chem. Rev.*, 104(1):293–346, October 2011.

[19] Jer-Shing Huang, Victor Callegari, Peter Geisler, Christoph Bruening, Johannes Kern, Jord C Prangsma, Xiaofei Wu, Thorsten Feichtner, Johannes Ziegler, Pia Weinmann, Martin Kamp, Alfred Forchel, Paolo Biagioni, Urs Sennhauser, and Bert Hecht. Atomically flat single-crystalline gold nanostructures for plasmonic nanocircuitry. *1004.1961*, April 2010.

List of Figures

List of Tables

Appendix A

Simulations: additional figures and tables

A.1 Maximum local field energy with $\Delta Y = 30$ nm.

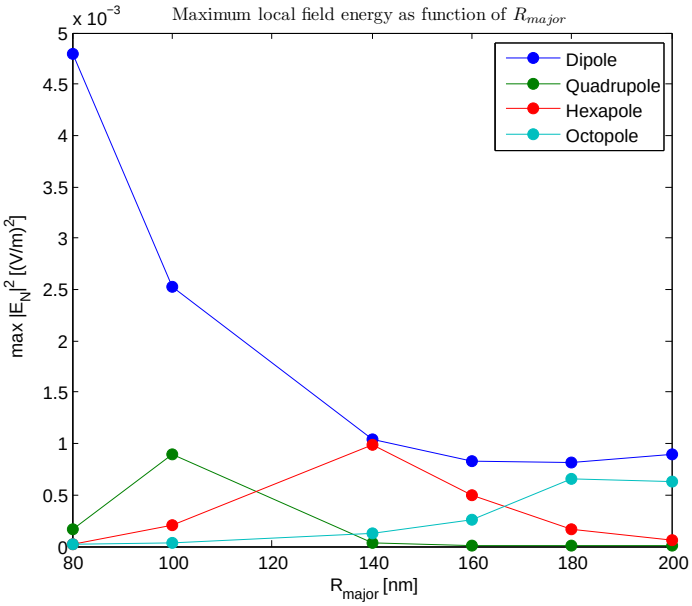

Figure A.1: Maximum local field energy with $\Delta Y = 30$ nm.

A.2 Maximum local field energy with $\Delta Y = 50$ nm.

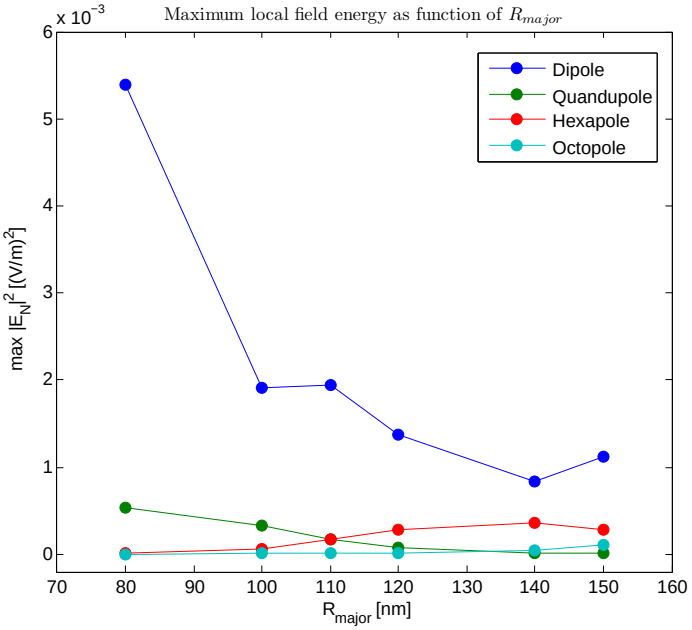

Figure A.2: Maximum local field energy with $\Delta Y = 50$ nm.

A.3 Local field energy for the bar and ring modes for $R_{major} = 97.5$ nm

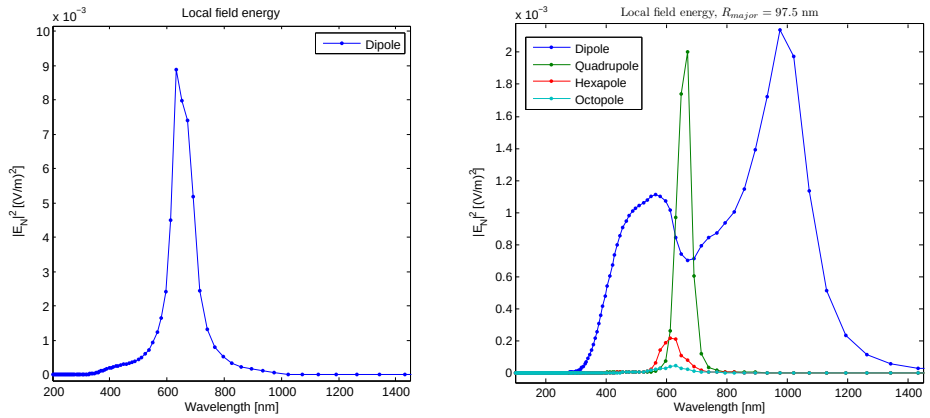

(a) Bar (b) Ring

Figure A.3: Local field energy for the bar and ring modes for $R_{major} = 97.5$ nm as function of wavelength.

A.4 Tables with bar ring resonances

The values for the center wavelength and FWHM linewidth have an estimated error of 15 nm. Q, H and O stand for a quadrupole, hexapole and octopole respectively. These correspond with a plasmon ring resonance of order $N = 2, 3, 4$.

$\Delta Y = 15$ nm			
	bar	ring	
R_{major} [nm]	$\lambda_0 \pm \Delta\lambda$ [nm]	type	$\lambda_0 \pm \Delta\lambda$ [nm]
80	655±50	Q	638±65
97.5	655±90	Q	658±55
115	655±60	Q	695±90
		H	625±70
132.5	655±90	H	640±50
150	655±90	H	660±50
		O	618±55
185	655±40	O	648±45
202.5	670±80	O	660±40

Table A.1: Center wavelength and FWHM linewidth of dipole bar mode and non-dipolar ring modes for $\Delta Y = 15$ nm.

$\Delta Y = 30$ nm			
	bar	ring	
R_{major} [nm]	$\lambda_0 \pm \Delta\lambda$ [nm]	type	$\lambda_0 \pm \Delta\lambda$ [nm]
80	638±45	Q	630±50
100	630±60	Q	660±60
		H	638±65
140	638±62	H	640±40
		O	610±50
160	635±50	H	673±25
		O	620±40
180	640±60	O	635±30
200	643±55	O	653±35

Table A.2: Center wavelength and FWHM linewidth of dipole bar mode and non-dipolar ring modes for $\Delta Y = 30$ nm.

$\Delta Y = 50$ nm			
	bar	ring	
R_{major} [nm]	$\lambda_0 \pm \Delta\lambda$ [nm]	type	$\lambda_0 \pm \Delta\lambda$ [nm]
80	633±55	Q	625±40
100	630±50	Q	653±55
110	633±45	Q	670±100
		H	615±50
120.5	630±60	H	623±45
140	630±50	H	638±35
		O	610±50
150	628±55	H	653±55
		O	613±45

Table A.3: Center wavelength and FWHM linewidth of dipole bar mode and non-dipolar ring modes for $\Delta Y = 50$ nm.

Appendix B

Schematic overview of setup

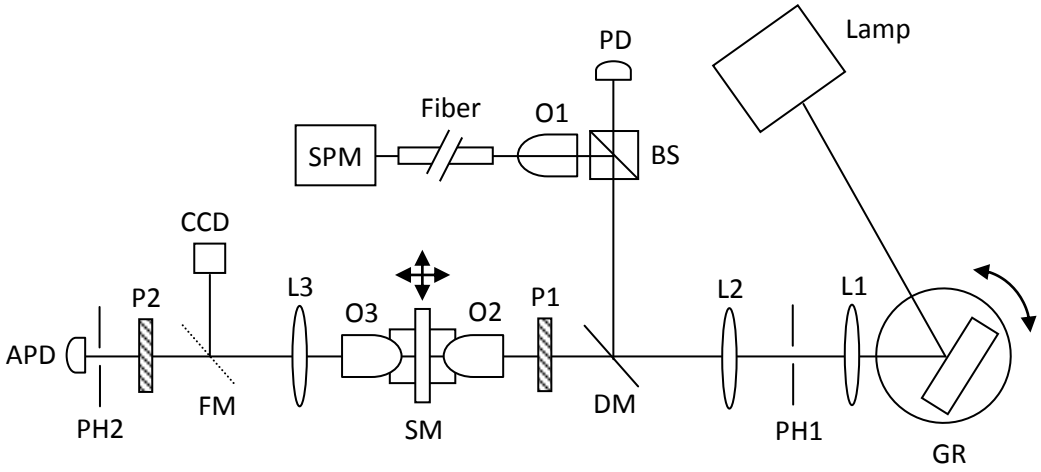

Abbreviation	meaning
APD	EG&G SPCM-AQ-160
AS	Adjustable slit
BS	50:50 beamsplitter
CCD	Pixelink CD camera
DM	D-shaped mirror
FM	Flip mirror
GR	Blazed grating on stepper rotation table, 1200 lines per mm
Lamp	Newport Apex Xe lamp
L1 & L2	Lens, f = 125 mm
L3	Achromatic doublet Lens, f = 120 mm
O1	Objective, 10x magnification
O2	Objective, Nikon M-Plan 40x 0.5 NA ELWD 210/0
O3	Objective, Zeiss Plan Neo-fluar 0.75 NA, ∞/0.17
P1 & P2	Thorlabs Linear film polarizer LPVIS
PD	photodiode PIN 10D
PH	Pinhole, 20 micrometer diameter
SM	Sample mount on a Smaract x,y,z MCS
SPM	Avantes Avaspec-3648 spectrometer